

Inferring the Isotropic-nematic Phase Transition with Generative Machine Learning

Eric R. Beyerle^{*1, a)} and Pratyush Tiwary^{*2, 3, b)}

¹⁾*Institute for Physical Science and Technology, University of Maryland, College Park, MD 20742, United States*

²⁾*Department of Chemistry and Biochemistry and Institute for Physical Science and Technology, University of Maryland, College Park, MD 20742, United States*

³⁾*University of Maryland Institute for Health Computing, Bethesda, MD 20852, United States*

(Dated: 29 October 2024)

Contemporary work implies generative machine learning models are capable of learning the phase behavior in condensed matter systems such as the Ising model. In this Letter, we utilize a score-based modeling procedure called Thermodynamic Maps to describe the isotropic-nematic phase transition in a melt of $N = 343$ calamitic Gay-Berne ellipsoids. When trained on samples generated by molecular dynamics simulation from a single temperature on either side of the phase transition, we demonstrate this generative machine learning approach infers information regarding the critical behavior and estimates effectively the nematic order parameter at sampled temperatures between the two training temperatures. These results demonstrate score-based models' ability to learn the physics of a non-trivial liquid crystalline phase transition driven by anisotropic interactions both entropic and energetic in nature.

Introduction— Modeling the phase transitions in liquid crystalline systems is important due to their contemporary use in electronic displays, organic electronics, thin-film thermometers, and other useful devices.^{1–3} In addition to their widespread practical applications, liquid crystals have been the subject of intense experimental, theoretical, and, recently, computational research because they display long-range order along only a single dimension, with a symmetry between that of disordered liquids and completely ordered solids.⁴ In general, liquid crystalline phase transitions are seen in systems composed of anisotropic particles or molecules, such as active rods⁵, lipids,^{6,7} and cyanobiphenyls in displays.^{3,8,9} The physics of liquid crystalline systems are modeled accounting for the constituent particles' anisotropy in both shape and inter-particle interactions.^{10–16} An early and successful approach to model not only liquid crystals, but more generally colloidal, anisotropic systems comes via the Gay-Berne (GB) potential,^{17,18} which has been used to study the behavior of a variety of colloidal systems for over 40 years.^{19–23} Its ability to model such a wide array of physical systems with computational and analytical efficiency makes the GB model highly useful despite its age.

Effectively an anisotropic Lennard-Jones interaction, the GB potential is parameterized by the relative orientation of the constituent ellipsoids, the ratio of the their long and short axes, and the distance between their cen-

ters of mass as follows:

$$U(\hat{u}_1, \hat{u}_2, r) = 4\epsilon(\hat{u}_1, \hat{u}_2, r) \left[\left(\frac{\sigma(\hat{u}_1, \hat{u}_2, \hat{r})}{r} \right)^{12} - \left(\frac{\sigma(\hat{u}_1, \hat{u}_2, \hat{r})}{r} \right)^6 \right], \quad (1)$$

where \hat{u}_1 and \hat{u}_2 specify the relative orientation of particles labeled 1 and 2 in a common reference frame; \hat{r} is the unit vector between the centers of the two ellipsoids; and r is the magnitude of the distance between their centers. The explicit forms of $\epsilon(\hat{u}_1, \hat{u}_2, r)$ and $\sigma(\hat{u}_1, \hat{u}_2, \hat{r})$ are given in the original paper,¹⁷ and interested parties are referred to its implementation in LAMMPS² for additional information regarding the theory and computational implementation of the GB potential. Explicit details regarding implementation of the potential in LAMMPS are given in the SI²⁴.

An extensive literature shows this system transitions among liquid crystalline states: isotropic, nematic, smectic, and cholesteric, depending on the thermodynamic conditions.^{25–28} Given the simple potential function but rich phase diagram, this model system has great use for the study of condensed matter systems sampling liquid crystalline states. Here, we narrow our focus to the isotropic-nematic phase transition, which is caused by the anisotropy of the GB ellipsoids and is responsible for many optical properties of liquid crystalline displays.

In Figures 1a,b we show representative configurations of the Gay-Berne melt in the isotropic and nematic phases, respectively. The global difference between the two is the breaking of the O_3 rotational symmetry along a protected axial direction called the director,⁴ which is superimposed as a blue, dashed arrow on three ellipsoids in Figure 1b). This orientational symmetry breaking pushes the system from a liquid phase to a liquid crystalline

^{a)}Electronic mail: eric.beyerle@bio.ku.dk

^{b)}Electronic mail: ptiwary@umd.edu

phase and is due to the anisotropic nature of the GB ellipsoids.

We focus on inferring the critical behavior of the isotropic-nematic phase transition given only equilibrium fluctuations in the isotropic and nematic states using an ML approach termed thermodynamic maps (TM).³⁰ A score-based approach, TM learns a map between distinct physical states, in this case the isotropic and nematic phases, and infers the physics behind transitioning between these states by learning a fluctuation-coupled backwards diffusion equation.^{30,31} A main finding of this Letter is TM’s ability to infer successfully the physics of the critical point, where sampling probability is its lowest, based on fluctuations gathered at only two temperatures, both far from the critical point: one temperature where the isotropic phase is stable and another where the nematic phase is stable.

With the contemporary availability of large training datasets generated through experiment or simulation, statistical techniques relying on machine learning approaches have become popular for identifying and studying phase transitions. These approaches range from shallow, linear ML methods such as PCA for learning the order parameter in condensed matter systems^{32–35}, to more sophisticated, generally non-linear approaches such as convolutional neural networks to identify structure^{36,37} and encoder-based neural networks to learn reaction coordinates for distinguishing phases.^{38–41} When using these types of ML approaches, the boundary between using models that are completely interpretable, but too simple to fit the observed data sufficiently well and models that are intractable but yield exceptional fits to the observations is sometimes difficult to straddle. Ideally, we desire a model balancing the bias-variance tradeoff⁴², being physically informed and interpretable yet expressive enough to fit the observed data.

The thermodynamic maps (TM) method we use is a type of generative machine learning architecture called a score-based model⁴³. These models are nonlinear, data-driven, machine-learned extensions of classical physics-based methods such as targeted free-energy perturbation⁴⁴ and annealed parallel tempering⁴⁵ that map between two probability distributions defined on the same space. Practically, the score-based model is trained to learn the score or the gradient of the target probability distribution by iteratively learning a noising schedule from an estimate of the target distribution to a normal distribution.^{43,46–51} The trained model effectively samples from the complicated and multimodal target distribution.

For spin systems, e.g. the Ising model, given samples from a wide range of temperatures, simpler ML models such as PCA and autoencoders can learn the critical behavior of the transition between the para- and ferromagnetic states.^{32,52–54} These calculations require spins from range of temperatures on both sides of the transition as well as at the critical point, reducing their appeal. However, using TM, a temperature-coupled score-based

model, we take one temperature on each side of the critical point and learn the critical behavior of the isotropic-nematic phase transition for a system of GB ellipsoids more effectively than other generative models. This approach guarantees that the ML model balances the bias-variance trade-off by using a complex architecture with sparse inputs to learn the physics at the critical point without overfitting the observed data. For these previous systems, the order parameter demarcating the disordered and ordered states is the global magnetization, a linear sum of the constituent spins. This is also true for previous application of TM to the Ising model.³⁰ Here, on the other hand, calculation of the nematic order parameter requires a non-linear transformation of the ellipsoid orientations, therefore requiring a non-linear modeling approach such as TM.

Theory and Methods– For a GB system comprising N particles, the nematic order parameter S is defined through an averaging of the local orientation of each GB particle:

$$S = \left\langle \frac{3 \cos^2(\theta) - 1}{2} \right\rangle := \frac{1}{N} \sum_i \left(\frac{3 \cos^2(\theta_i) - 1}{2} \right), \quad (2)$$

where $\cos(\theta_i) = \hat{u}_i \cdot \hat{n}$ is the cosine of the angle between the orientation vector of GB particle i , \hat{u}_i , and the director vector \hat{n} . Drawing an analogy to the magnetization order parameter, M , of the Ising model, which is defined as $M = \frac{1}{N} \sum_i s_i$, where $s_i \in \{-1, 1\}$ is the spin at lattice site i , the mapping between the GB and discrete spin model is performed using

$$s_i \longleftrightarrow \cos^2(\hat{u}_i \cdot \hat{n}) = \cos^2(\theta_i) \quad (3)$$

$$M \longleftrightarrow S := \frac{3}{2} M_{\text{GB}} + \text{const.}; \quad M_{\text{GB}} := \frac{1}{N} \sum_i \cos^2(\theta_i). \quad (4)$$

The fundamental difference between Ising spins and GB unit orientations is the GB model’s invariance to reflections normal to the director axis specified by \hat{n} , which limits the range of M_{GB} to $[0, 1]$ instead of $M \in [-1, 1]$ in the Ising model. The orientational invariance introduced by taking the dot product changes how the order parameter is calculated from a simple linear average over spins to the average of the square of a cosine function. Analytically, the change of variables introduced in eqs. 3 and 4 provides a mapping between the models, but this non-linear mapping is non-trivial when learned by an ML model. Crucially, this indicates linear approaches cannot learn this order parameter without at least the kernel trick.⁵⁵

The advantage of using a generative model such as a diffusion model over ML classifier methods such as convolutional neural networks or bottleneck-based approaches such as PCA and autoencoders is the ability of the diffusion model to generate novel samples at state points not seen during training. To use TM to infer the critical

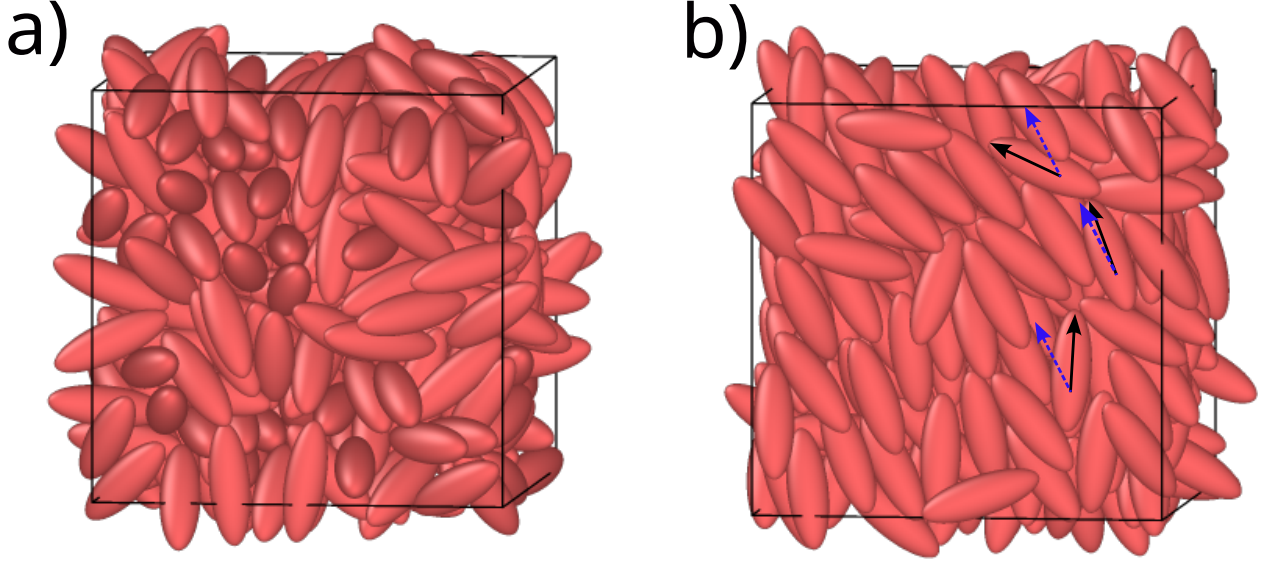


FIG. 1: The two phases sampled by the GB system at the phase points studied in this Letter: a) isotropic and b) nematic. Both snapshots are generated using OVITO.²⁹ For the nematic phase in panel b), we show three example orientation unit vectors, \hat{u}_i , as black arrows for three ellipsoids. For these labeled ellipsoids, we also superimpose the approximate director vector, \hat{n} , as a dashed, blue arrow.

behavior, the model is trained to learn a noising schedule that allows inference of structures generated at a given bath temperature, which is coupled to the fluctuations of the observables. While trained on the one temperature and the associated fluctuations on each side of the critical point, the TM can generalize to unseen temperatures between the two, including the critical point. Thus, TM mixes information from the simulations performed at different temperatures and generates novel samples at a requested and previously unseen temperatures.

Formally, TM learns a map $\mathcal{M}_\theta : \mathbb{R}^{2N} \rightarrow \mathbb{R}^{2N}$ from the $2N$ -dimensional space of input configurations and corresponding fluctuations to itself using a neural net-

work with parameters θ . We input the orientation vector $\mathbf{x}_i := \hat{u}_i = (u_i^x, u_i^y, u_i^z)$ for each particle i as a one-dimensional array to a one-dimensional convolutional Unet⁵⁶ architecture. We complement the N -dimensional \mathbf{x} with another vector $\boldsymbol{\beta}$ of dimensionality N that quantifies the fluctuations of the input features at a given bath temperature. We refer to the vector $\boldsymbol{\beta}^{-1}$ as a temperature space, compared to the bath temperature, a scalar. The TM learns the mapping \mathcal{M}_θ that estimates the gradient of the log probability of the sampled data, $\nabla_{\mathbf{x}, \boldsymbol{\beta}^{-1}} \log(p(\mathbf{x}, \boldsymbol{\beta}^{-1}))$, also known as the score. This satisfies the following forward and backward diffusion equations (or noising and denoising diffusion models):

$$\begin{pmatrix} d\mathbf{x} \\ d\boldsymbol{\beta}^{-1} \end{pmatrix} = -\frac{1}{2}\sigma(t) \begin{pmatrix} \mathbf{x} \\ \boldsymbol{\beta}^{-1} \end{pmatrix} dt + \sqrt{\sigma(t)} \begin{pmatrix} \sqrt{\boldsymbol{\beta}_0^{-1}} \\ \mathbf{1} \end{pmatrix} d\mathbf{w} \quad \text{and} \quad (5)$$

$$\begin{pmatrix} d\mathbf{x} \\ d\boldsymbol{\beta}^{-1} \end{pmatrix} = -\frac{1}{2}\sigma(t) \left[\begin{pmatrix} \mathbf{x} \\ \boldsymbol{\beta}^{-1} \end{pmatrix} + \begin{pmatrix} \mathbf{s}_\theta(\mathbf{x}, t) \\ \mathbf{s}_\theta(\boldsymbol{\beta}^{-1}, t) \end{pmatrix} \right] dt + \sqrt{\sigma(t)} \begin{pmatrix} \sqrt{\boldsymbol{\beta}_0^{-1}} \\ \mathbf{1} \end{pmatrix} d\mathbf{w}, \quad (6)$$

where $\mathbf{w} \sim \mathcal{N}(0, \mathbf{I})$ and $\sigma(t)$ is the noise schedule of the diffusion model.⁵⁷ $\mathbf{s}_\theta(\mathbf{x}, t)$ is the score learned by the diffusion model in the input feature space and $\mathbf{s}_\theta(\boldsymbol{\beta}^{-1}, t)$ is the score learned in the space of the input temperatures. Furthermore, $\boldsymbol{\beta}_0$ refers to the prior estimate of the fluctuations at the two bath temperatures in the training data, which are calculated as the sample variance from

the input MD data. The additional channel containing information connecting the fluctuations to the temperature allows the TM architecture to infer configurations at novel temperatures unseen during training.⁴⁷ Details regarding parametrization and training the TM are given in the SI²⁴ and the associated GitHub repository for this Letter.⁵⁸

The global nematic order parameter \mathcal{S} is estimated from the input features, which are the orientations \hat{u}_i for each GB particle, by calculating the largest eigenvalue of the orientation tensor $Q = \frac{1}{N} \sum_i \hat{u}_i \otimes \hat{u}_i - \frac{1}{3}I$:

$$\mathcal{S} = \frac{3}{2} \max(\rho(Q)), \quad (7)$$

where $\rho(Q)$ denotes the eigenvalue spectrum of Q ⁵⁹ and $I \in \mathbb{Z}^{N \times N}$ is an $N \times N$ identity matrix. The TM model is trained on particle orientations from two temperatures, one below the critical temperature and one above the critical temperature. Then, the trained TM model infers orientations $\hat{u}_{i, \text{TM}}$ at any given temperature. These inferred orientation are used to calculate Q and \mathcal{S} using eq. 7

We model this weakly first-order phase transition between the isotropic and nematic phases in a GB(3,5,2,1) system^{22,60} by performing molecular dynamics (MD) simulations of a melt of $N = 343$ GB ellipsoids in the NVT ensemble at temperatures ranging from $T^* = 0.2$ to $T^* = 2.4$, where T^* is the reduced Lennard-Jones (LJ) units of temperature, $T^* = k_B T / \epsilon$, with ϵ the side-side well-depth in the GB potential. At this density and over this span of temperatures, the GB system undergoes a transition from the nematic to isotropic phase at the critical temperature of $T_C^* \approx 1.74$.

All measured and calculated quantities are reported in reduced LJ units. Phase points are generated along the $\rho^* = 0.35$ iso-density line. All simulations are performed using the 10 March 2021 build of LAMMPS.⁶¹

Simulations are initiated by placing the GB ellipsoids in a box of volume $V = 34300\sigma$ and ramping the temperature from $T^* = 0.1$ to $T^* = 3.0$ using a Nosé-Hoover thermostat.⁶² Next, the simulation box is compressed at $T^* = 3.0$ using a Nosé-Hoover barostat to a reduced density of $\rho^* = 0.35$. When that density is reached, the system is annealed to the desired T^* before running a production run of 10^6 integration steps at the desired state point. The integration timestep is $t^* = 0.0015$, giving a total simulation length of 1.5×10^3 . The scaling exponents for GB potential are $\nu = 1.0$ and $\mu = 2.0$; the long axis of the GB ellipsoid is 3.0σ while the short axis is 1.0σ for an aspect ratio of 3. Finally, the side-side interactions are set at 1.0ϵ while the end-end interactions are set at 0.2ϵ , making the system studied a GB(3, 5, 2, 1) in the conventional nomenclature¹⁰. Details regarding the exact implementation of the potential in LAMMPS are given in the SI.²⁴

Results– The main result of this Letter is the quantitative and qualitative agreement between the global nematic order parameter \mathcal{S} across temperatures calculated from MD simulations, shown in Figure 2. The TM model making the predictions is trained on only two temperatures far from the critical point. To generate the TM results, 9000 sample configurations at $T^* = 1.0$ and $T^* = 2.0$ are input to the diffusion model, and 10000 configurations are generated at all temperatures shown in Figure 2. The agreement between the nematic order parameter \mathcal{S} cal-

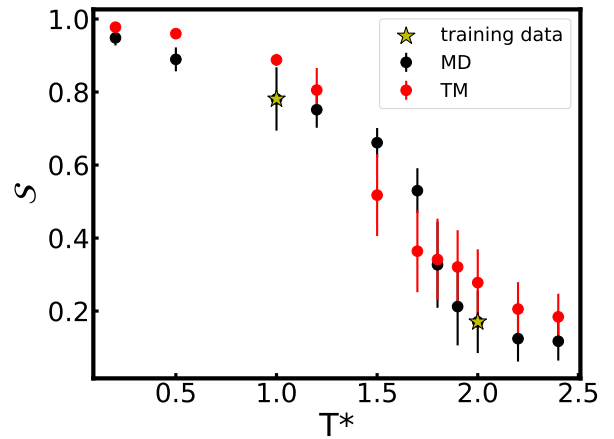


FIG. 2: Plot of the nematic order parameter \mathcal{S} calculated from MD (black circles) and the inferred values from trained TM (red circles). The TM results are inferred by training on MD data at the two temperatures highlighted by the yellow stars. Error bars for MD are one standard deviation of \mathcal{S} calculated using 9000 frames from the simulation at the given T^* while the error bars for the TM are taken from 10000 samples inferred at each T^* . Error bars for all points correspond to one sample standard deviation.

culated from MD and TM are within error of each other at most temperatures, including temperatures above the highest training temperature $T^* = 2.0$. The model struggles to predict the value of \mathcal{S} near the critical temperature of $T_C^* \approx 1.74$. Even right at the critical temperature the agreement is remarkable when accounting for uncertainty. Furthermore, we are still able to calculate scaling laws in the critical region that agree with those from MD (Figure 4 and the agreement between the MD and TM free-energy surfaces near the critical point is relatively good (Figure 3).

As a control, we use a principal component analysis (PCA)⁶³ and variational autoencoder (VAE)⁶⁴ to learn the nematic order parameter by inputting the projections of each ellipsoid onto the director, $\cos(\theta_i)$, at *all temperatures* into the PCA and VAE architectures. In the SI, we demonstrate that even inputting information at all temperatures, as opposed to only 2 temperatures used to train TM, the linear PCA does not learn any significant physics, always returning a nematic order parameter within uncertainty of a null value.

The VAE learns an order parameter decaying from the nematic to the isotropic states as temperature increases, but with large error bars, as with PCA. Since the calculation of the order parameter is a nonlinear transformation, it is expected PCA fails to learn a mapping from orientational projection to the order parameter. However, for the VAE, it is a bit surprising that it does not do a better job learning the order parameter even though it utilizes a nonlinear encoder with ReLU activation functions.

Although the TM cannot match *exactly* the order parameter in the critical region, its performance is vastly superior to the competing PCA and VAE generative mod-

els. This result is significantly different from the Ising model, where all three methods effectively learn the phase transition.^{30,32} We emphasize that since the PCA and VAE fail to reproduce $\mathcal{S}(T^*)$, even when trained *on all temperatures*, and they completely fail to reproduce critical behavior.

The TM algorithm's ability to match the one-dimensional free-energy surface along the \mathcal{S} order parameter as a function of T^* is shown in Figure 3. For temperatures above and below the critical temperature, the TM always predicts the correct phase: isotropic ($\mathcal{S} \lesssim 0.5$) above the critical temperature and nematic ($\mathcal{S} > 0.5$) below it. For state points sampled below the critical temperature, the TM approach systematically predicts that the GB melt is more ordered, $\mathcal{S}_{\text{TM}} \geq \mathcal{S}_{\text{MD}}$, compared to the reference MD simulation. This effect could be due to the sensitivity of the use of the dot product in the calculation of the nematic order parameter: practically, there is little physical difference between two GB melts with $\mathcal{S} = 0.8$ and $\mathcal{S} = 0.9$ when \mathcal{S} is relevant slow variable.

The free-energy profiles surrounding the transition state are in reasonable agreement with the MD results, with substantial overlapping support between the TM and MD wells, although the TM approach misses some subtleties within the free-energy basin at each temperature. For temperatures above the critical value, the TM method systematically predicts the free-energy minimum is located at a higher value of the nematic order parameter compared to the reference MD simulation, the same phenomenon observed at temperatures below the critical value. The cause of the systematic bias toward higher values of the nematic OP compared to the reference MD simulation is unknown and potential fodder for further study. The only exception to this trend is in the vicinity of the critical point, which is partially elucidated next.

The critical behavior is predicted by fitting scaling laws in the reduced temperature $\tau = (T^* - T_C^*)/T_C^*$ for the nematic order parameter \mathcal{S} as follows:

$$\mathcal{S} \sim \left| \frac{T^* - T_C^*}{T_C^*} \right|^{\mathcal{B}} = |\tau|^{\mathcal{B}} \quad (8)$$

at ranges of T^* exclusively above the critical temperature of $T_C^* \approx 1.74$. Figure 4 compares the scaling laws calculated using the MD and generated TM data. Fitting the branch of the \mathcal{S} versus T^* curve where $T^* > T_C^*$, we report the calculated scaling exponents \mathcal{B} in Table I. We see \mathcal{B} is in excellent agreement between the TM and MD predictions.

Thus, we conclude the TM method can infer some physics occurring at the critical temperature, as given by the matching predictions for the scaling exponent in Table I.

Finally, since the TM algorithm, as currently implemented, does not map from the full configuration space of the GB system onto itself, we use a nearest neighbor mapping technique to recover approximate potential energies of inferred TM configurations at each temperature. We assign energies by calculating the minimum distance

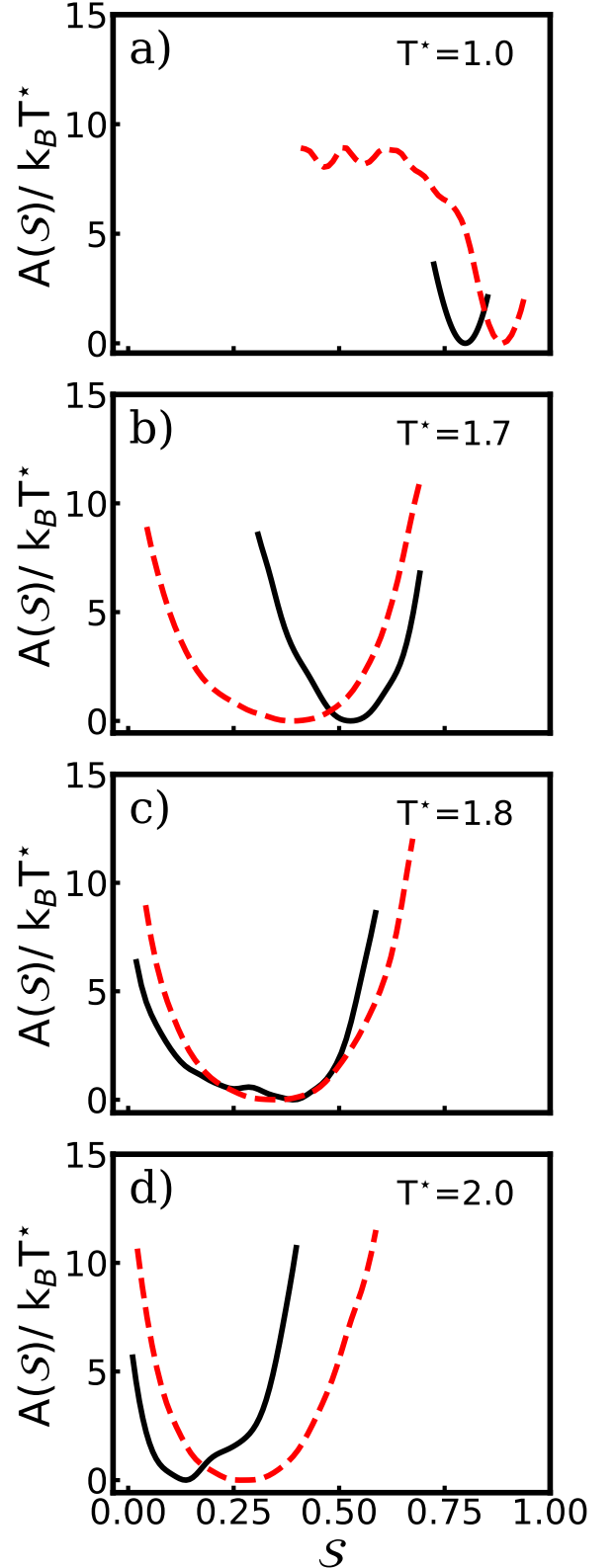


FIG. 3: a)-d): Plots of the free-energy along the nematic order parameter \mathcal{S} calculated from the MD (black) and TM (red, dashed) samples at the reduced temperature given in each inset. The temperature increases monotonically going from top to bottom through the subplots. This same plot over a wider sampling of temperatures is given in the SI.²⁴

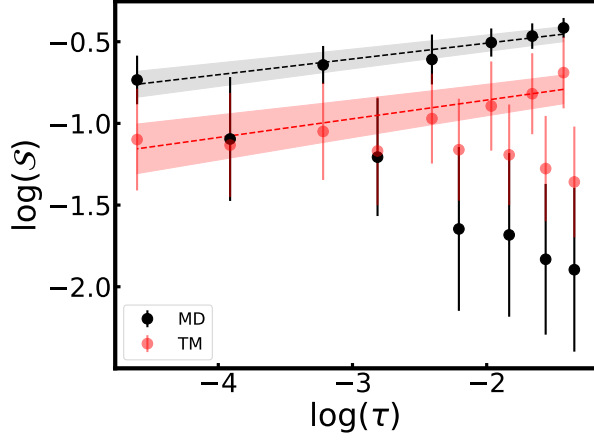


FIG. 4: Log-log plot of S versus τ with linear fits to the points above the critical temperature shown for both MD (black, dashed line) and TM (red, dashed line) data. Shaded regions show the error in the linear fit, as calculated using the curve fit optimization function in the Python scipy library.⁶⁵ Error bars for the MD and TM samples at each temperature are calculated using propagation of error⁶⁶ from the originally calculated values of S .

TABLE I: Scaling exponents for the nematic order parameter.

MD	TM
β 0.10 ± 0.01^a	0.11 ± 0.03^a

^aUncertainties are reported from the curve fitting algorithm used from the Python scipy library.⁶⁵

between a given TM configuration and one in the MD trajectory at the given, sampled temperature. We define the distance between a specified pair of TM and MD configurations as the negative sum of the dot product of the ellipsoid orientations between the two configurations. Formally, the potential energy of TM sample n , $U_{\text{TM}}(k)$, is defined as

$$U_{\text{TM}}(k) = U \left(\underset{\mathbf{x}(m) \in \mathbf{X}}{\operatorname{argmin}} \left(- \sum_{i=1}^N |\hat{u}_i(m) \cdot \hat{u}_i^{\text{TM}}(k)| \right) \right), \quad (9)$$

where $U \left(\underset{\mathbf{x}(m) \in \mathbf{X}}{\operatorname{argmin}} \dots \right)$ denotes the optimization of the distance between the TM-inferred configurations $\hat{\mathbf{x}}(k) = (\hat{u}_1^{\text{TM}}(k), \hat{u}_2^{\text{TM}}(k), \dots, \hat{u}_N^{\text{TM}}(k))$ and the MD configurations $\mathbf{x}(m) = (\hat{u}_1(m), \hat{u}_2(m), \dots, \hat{u}_N(m))$ over all inferred samples k and all MD frames m at a given bath temperature. The TM energy of sample k , $U_{\text{TM}}(k)$, is set equal to the MD frame m with which it has the lowest negative sum of dot products between ellipsoid orientational vectors. In the limit where the inputs and outputs of the TM algorithm are the full configuration space of the system, the mapping is exact.

While the energy-matching procedure in Eq. 9 neglects the distance dependence in the GB potential, since the

system is largely incompressible at $\rho^* = 0.35$, we find this mapping procedure in the reduced space of ellipsoid orientations gives reasonable agreement with the MD energies, even at the critical point, as shown by the plot of energy against temperature in Figure 5a.

We use estimate the heat capacity, $C_v \approx \Delta U / \Delta T^*$, from the mapped energies and compare it to the heat capacities measured in the reference MD simulations. For C_v calculated from the MD and mapped TM energies, there is no jump at the critical point, in contrast to the Ising model, where the energy changes sharply at the critical point.^{30,67} The gradual change in energy with temperature means there is no peak in C_v at T^* (Figures 5b and S3), and scaling exponents are within error of zero (Figure S3 and Table S1).

This behavior of C_v disagrees with data reported in e.g. Ref. 68 where there is a clear peak in the heat capacity at the isotropic-nematic transition point. The discrepancy between our qualitative results for both the potential energy and heat capacity curves stem from both the different parameterization of the GB potential and finite-size effects caused by different system sizes used in this study compared to Ref. 68. Indeed, for the Lebwohl-Lasher model, which is the lattice equivalent of the GB system studied here, the peak in the heat capacity is a strong function of system size.⁶⁹

Conclusions— In this Letter, we apply a generative, score-matching framework, thermodynamic maps (TM), to infer isotropic-nematic critical behavior in a system of $N=343$ Gay-Berne (GB) ellipsoids. Training on single phase points on either side of the critical temperature, we infer behavior in the neighborhood of the critical point, as indicated by the agreement between the nematic order parameter (Figure 2) and its scaling exponent at criticality (Figure 4 and Table I).

These results imply the TM method is applicable to non-trivial (i.e. non-Ising) condensed matter systems possessing long-ranged and anisotropic interactions. Such modeling is exceptionally useful in this case since we find that simpler generative modelling procedures such as principal component analysis and the variational autoencoder cannot effectively discriminate the isotropic and nematic phases as successfully as TM even when the ellipsoid orientations are pre-processed to introduce non-linearity *a priori* (Figure S2). This discrepancy implies the TM's diffusion model, which is effectively a stacked autoencoder⁷⁰, is a sufficiently universal approximator of the nematic order parameter from the orientations alone. That is, the TM is able to learn the cosine, squaring, and averaging function to calculate the nematic order parameter from the orientations alone, unlike PCA and the nonlinear VAE. Thus, while a simple model superficially similar to a three-dimensional spin model, the physics of the GB system's liquid crystalline phase transition differs fundamentally from a spin model. Physically, the observation is due to the different symmetries broken for the classical, three-dimensional Heisenberg spin model and the isotropic-nematic phase transition in colloids.⁴

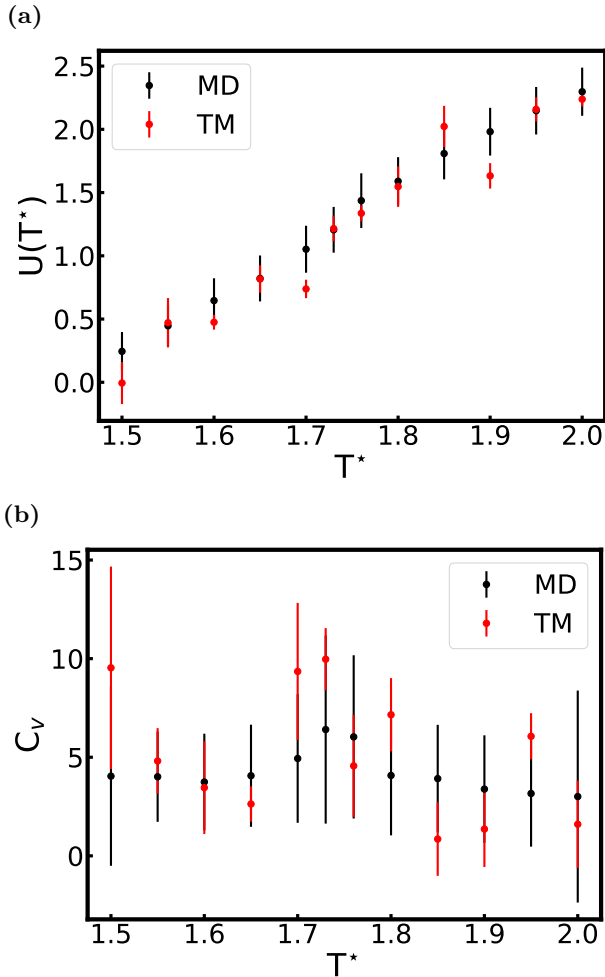


FIG. 5: a) Comparison of the average potential energy at each simulated temperature surrounding the critical region from the reference MD simulations (black) and the inferred energies from the TM approach (red) calculated using the nearest neighbor mapping procedure. Error bars in both cases are given by one standard deviation calculated from the sample variance at each temperature. b) Heat capacity for the reference MD (black) and TM (red) at each simulated temperature surrounding the critical region. The heat capacities for the TM samples are calculated using the mapped energies shown in a). Error bars in both cases are given by one standard deviation calculated from the sample variance at each temperature.

A limitation of this work is the small system size, corresponding to a $7 \times 7 \times 7$ lattice. We select this size due to previous use²² and computational feasibility. Finite-size effects are obvious when inspecting the asymmetry and rounding in the plot of order parameter versus temperature.^{71,72} While an issue when comparing the results to theory, our analysis is self-consistent since we compare to MD results. The TM successfully infers some physics at unseen state points despite the system's distance from the infinite size thermodynamic limit.

Since the current implementation of the TM method utilizes the fundamental connection between fluctuations

in the relevant degrees of freedom and the system's temperature, we are not able to examine the density-driven nematic-smectic liquid crystalline phase transition.⁷³ Updating the TM implementation using a tilted ensemble assumption^{74,75} should allow for a similar treatment of such density-driven phase transitions.

Acknowledgment— This work is entirely supported by the US Department of Energy, Office of Science, Basic Energy Sciences, CPIMS Program, under Award DE-SC0021009. We thank UMD HPC's Zaratan and NSF ACCESS (project CHE180027P) for computational resources. P.T. is currently an investigator at the University of Maryland-Institute for Health Computing, which is supported by funding from Montgomery County, Maryland and The University of Maryland Strategic Partnership: MPowering the State, a formal collaboration between the University of Maryland, College Park and the University of Maryland, Baltimore.

- ¹Pierre-Gilles De Gennes and Jacques Prost. *The physics of liquid crystals*. Number 83. Oxford university press, 1993.
- ²W. Michael Brown, Matt K. Petersen, Steven J. Plimpton, and Gary S. Grest. Liquid crystal nanodroplets in solution. *The Journal of Chemical Physics*, 130(4):044901, 01 2009.
- ³Denis Andrienko. Introduction to liquid crystals. *Journal of Molecular Liquids*, 267:520–541, 2018. Special Issue Dedicated to the Memory of Professor Y. Reznikov.
- ⁴P. M. Chaikin and T. C. Lubensky. *Principles of Condensed Matter Physics*. Cambridge University Press, 1995.
- ⁵Amin Doostmohammadi, Jordi Ignés-Mullol, Julia M. Yeomans, and Francesc Sagues. Active nematics. *Nature Communications*, 9, August 2018.
- ⁶Chandrashekar V Kulkarni. Lipid crystallization: from self-assembly to hierarchical and biological ordering. *Nanoscale*, 4(19):5779–5791, 2012.
- ⁷V. Luzzati, H. Mustacchi, and A. Skoulios. Structure of the liquid-crystal phases of the soap-water system: Middle soap and neat soap. *Nature*, 180(4586):600–601, September 1957.
- ⁸Mattia Felice Palermo, Antonio Pizzirusso, Luca Muccioli, and Claudio Zannoni. An atomistic description of the nematic and smectic phases of 4-n-octyl-4' cyanobiphenyl (8CB). *The Journal of Chemical Physics*, 138(20):204901, 05 2013.
- ⁹Giustiniano Tiberio, Luca Muccioli, Roberto Berardi, and Claudio Zannoni. Towards in silico liquid crystals. realistic transition temperatures and physical properties for n-cyanobiphenyls via molecular dynamics simulations. *ChemPhysChem*, 10(1):125–136, 2009.
- ¹⁰M. A. Bates and G. R. Luckhurst. *Computer Simulation of Liquid Crystal Phases Formed by Gay-Berne Mesogens*, pages 65–137. Springer Berlin Heidelberg, Berlin, Heidelberg, 1999.
- ¹¹Friederike Schmid and Nguyen H Phuong. Spatial order in liquid crystals: Computer simulations of systems of ellipsoids. In *Morphology of Condensed Matter: Physics and Geometry of Spatially Complex Systems*, pages 172–186. Springer, 2002.
- ¹²G. R. Luckhurst, R. A. Stephens, and R. W. Phippen. Computer simulation studies of anisotropic systems. xix. mesophases formed by the gay-berne model mesogen. *Liquid Crystals*, 8:451–464, 1990.
- ¹³Anja Humpert. *Computer Simulations of Liquid Crystals*. PhD thesis, University of Warwick, 2016.
- ¹⁴Jean-Pierre Hansen and Ian Ranald McDonald. *Theory of simple liquids: with applications to soft matter*. Academic press, 2013.
- ¹⁵C Zannoni. An introduction to the molecular dynamics method and to orientational dynamics in liquid crystals. *The molecular dynamics of liquid crystals*, pages 139–169, 1994.
- ¹⁶Vyas Ramasubramani, Thi Vo, Joshua A. Anderson, and Sharon C. Glotzer. A mean-field approach to simulating

- anisotropic particles. *The Journal of Chemical Physics*, 153(8):084106, 2020.
- ¹⁷J. G. Gay and B. J. Berne. Modification of the overlap potential to mimic a linear site-site potential. *The Journal of Chemical Physics*, 74(6):3316–3319, 03 1981.
 - ¹⁸R. Everaers and M. R. Ejtehadi. Interaction potentials for soft and hard ellipsoids. *Physical Review E - Statistical Physics, Plasmas, Fluids, and Related Interdisciplinary Topics*, 67:8, 2003.
 - ¹⁹Prasanth P Jose and Biman Bagchi. Anomalous viscoelasticity near the isotropic-nematic phase transition in liquid crystals. *The Journal of chemical physics*, 121(14):6978–6985, 2004.
 - ²⁰PJ Andrew et al. Monte carlo investigations of a gay—berne liquid crystal. *Journal of the Chemical Society, Faraday Transactions*, 89(22):4069–4078, 1993.
 - ²¹Michael P Allen, Julian T Brown, and Mark A Warren. Computer simulation of liquid crystals. *Journal of Physics: Condensed Matter*, 8(47):9433, 1996.
 - ²²Wenduo Chen, Youliang Zhu, Fengchao Cui, Lunyang Liu, Zhaoyan Sun, Jizhong Chen, and Yunqi Li. Gpu-accelerated molecular dynamics simulation to study liquid crystal phase transition using coarse-grained gay-berne anisotropic potential. *PLOS ONE*, 11(3):1–21, 03 2016.
 - ²³Gert Jan Vroege and Henk NW Lekkerkerker. Phase transitions in lyotropic colloidal and polymer liquid crystals. *Reports on Progress in Physics*, 55(8):1241, 1992.
 - ²⁴See supplemental material at [URL] for further simulation details.
 - ²⁵Enrique De Miguel, Luis F. Rull, Manoj K. Chalam, and Keith E. Gubbins. Liquid crystal phase diagram of the gay-berne fluid. *Molecular Physics*, 74(2):405–424, 1991.
 - ²⁶Enrique De Miguel, Luis F. Rull, and Keith E. Gubbins. Dynamics of the gay-berne fluid. *Physical Review A*, 45:3813–3822, 1992.
 - ²⁷Nishant Birdi, Tom L Underwood, Nigel B Wilding, Sanjay Puri, and Varsha Banerjee. Equilibrium phases and domain growth kinetics of calamitic liquid crystals. *Physical Review E*, 105(2):024706, 2022.
 - ²⁸Kazuaki Z Takahashi, Takeshi Aoyagi, and Jun-ichi Fukuda. Multistep nucleation of anisotropic molecules. *Nature communications*, 12(1):5278, 2021.
 - ²⁹Alexander Stukowski. Visualization and analysis of atomistic simulation data with OVITO—the Open Visualization Tool. *Modelling and Simulation in Materials Science and Engineering*, 18(1), JAN 2010.
 - ³⁰Lukas Herron, Kinjal Mondal, John S. Schneekloth, and Pratyush Tiwary. Inferring phase transitions and critical exponents from limited observations with Thermodynamic Maps. *arXiv e-prints*, page arXiv:2308.14885, August 2023.
 - ³¹Brian DO Anderson. Reverse-time diffusion equation models. *Stochastic Processes and their Applications*, 12(3):313–326, 1982.
 - ³²Sebastian J Wetzal. Unsupervised learning of phase transitions: From principal component analysis to variational autoencoders. *Phys. Rev. E*, 96(2):022140, 2017.
 - ³³R. B. Jadrich, B. A. Lindquist, W. D. Piñeros, D. Banerjee, and T. M. Truskett. Unsupervised machine learning for detection of phase transitions in off-lattice systems. II. Applications. *The Journal of Chemical Physics*, 149(19):194110, 11 2018.
 - ³⁴R. B. Jadrich, B. A. Lindquist, and T. M. Truskett. Unsupervised machine learning for detection of phase transitions in off-lattice systems. I. Foundations. *The Journal of Chemical Physics*, 149(19):194109, 11 2018.
 - ³⁵Wenjian Hu, Rajiv RP Singh, and Richard T Scalettar. Discovering phases, phase transitions, and crossovers through unsupervised machine learning: A critical examination. *Physical Review E*, 95(6):062122, 2017.
 - ³⁶Dimitrios Bachtis, Gert Aarts, and Biagio Lucini. Mapping distinct phase transitions to a neural network. *Physical Review E*, 102(5):053306, 2020.
 - ³⁷Soo Min Oh, Kwangjong Choi, and B Kahng. Machine learning approach to percolation transitions: global information. *Journal of Statistical Mechanics: Theory and Experiment*, 2023(8):083210, 2023.
 - ³⁸Jianmin Shen, Shiyang Chen, Feiyi Liu, Youju Liu, and Wei Li. Learning phase transitions by siamese neural network. *arXiv preprint arXiv:2405.16769*, 2024.
 - ³⁹Jianmin Shen, Feiyi Liu, Shiyang Chen, Dian Xu, Xiangna Chen, Shengfeng Deng, Wei Li, Gábor Papp, and Chunbin Yang. Transfer learning of phase transitions in percolation and directed percolation. *Physical Review E*, 105(6):064139, 2022.
 - ⁴⁰Burak Çivitcioglu, Rudolf A Römer, and Andreas Honecker. Phase determination with and without deep learning. *arXiv preprint arXiv:2403.09786*, 2024.
 - ⁴¹Julian Arnold, Frank Schäfer, Alan Edelman, and Christoph Bruder. Mapping out phase diagrams with generative classifiers. *Phys. Rev. Lett.*, 132:207301, May 2024.
 - ⁴²Robert T McGibbon, Christian R Schwantes, and Vijay S Pande. Statistical model selection for markov models of biomolecular dynamics. *The Journal of Physical Chemistry B*, 118(24):6475–6481, 2014.
 - ⁴³Jiaming Song, Chenlin Meng, and Stefano Ermon. Denoising diffusion implicit models. *arXiv preprint arXiv:2010.02502*, 2020.
 - ⁴⁴Christopher Jarzynski. Targeted free energy perturbation. *Physical Review E*, 65(4):046122, 2002.
 - ⁴⁵Radford M Neal. Annealed importance sampling. *Statistics and computing*, 11:125–139, 2001.
 - ⁴⁶Juan Viguera Diez, Sara Romeo Atance, Ola Engkvist, and Simon Olsson. Generation of conformational ensembles of small molecules via surrogate model-assisted molecular dynamics. *Machine Learning: Science and Technology*, 5(2):025010, 2024.
 - ⁴⁷Yihang Wang, Lukas Herron, and Pratyush Tiwary. From data to noise to data for mixing physics across temperatures with generative artificial intelligence. *Proceedings of the National Academy of Sciences*, 119(32):e2203656119, 2022.
 - ⁴⁸Jascha Sohl-Dickstein, Eric Weiss, Niru Maheswaranathan, and Surya Ganguli. Deep unsupervised learning using nonequilibrium thermodynamics. In *International Conference on Machine Learning*, pages 2256–2265. PMLR, 2015.
 - ⁴⁹Sam Bond-Taylor, Adam Leach, Yang Long, and Chris G Willcocks. Deep generative modelling: A comparative review of vaes, gans, normalizing flows, energy-based and autoregressive models. *IEEE transactions on pattern analysis and machine intelligence*, 44(11):7327–7347, 2021.
 - ⁵⁰Arpit Bansal, Eitan Borgnia, Hong-Min Chu, Jie Li, Hamid Kazemi, Furong Huang, Micah Goldblum, Jonas Geiping, and Tom Goldstein. Cold diffusion: Inverting arbitrary image transforms without noise. *Advances in Neural Information Processing Systems*, 36, 2024.
 - ⁵¹Yang Song, Jascha Sohl-Dickstein, Diederik P Kingma, Abhishek Kumar, Stefano Ermon, and Ben Poole. Score-based generative modeling through stochastic differential equations. *arXiv preprint arXiv:2011.13456*, 2020.
 - ⁵²Lei Wang. Discovering phase transitions with unsupervised learning. *Physical Review B*, 94(19):195105, 2016.
 - ⁵³David Yevick. Variational autoencoder analysis of ising model statistical distributions and phase transitions. *The European Physical Journal B*, 95(3):56, Mar 2022.
 - ⁵⁴Francesco D’Angelo and Lucas Böttcher. Learning the ising model with generative neural networks. *Physical Review Research*, 2(2):023266, 2020.
 - ⁵⁵Bernhard Schölkopf, Alexander Smola, and Klaus-Robert Müller. Nonlinear component analysis as a kernel eigenvalue problem. *Neural computation*, 10(5):1299–1319, 1998.
 - ⁵⁶Olaf Ronneberger, Philipp Fischer, and Thomas Brox. U-net: Convolutional networks for biomedical image segmentation. In Nassir Navab, Joachim Hornegger, William M. Wells, and Alejandro F. Frangi, editors, *Medical Image Computing and Computer-Assisted Intervention – MICCAI 2015*, pages 234–241, Cham, 2015. Springer International Publishing.
 - ⁵⁷Jonathan Ho, Ajay Jain, and Pieter Abbeel. Denoising diffusion probabilistic models. *Advances in Neural Information Processing*

- Systems*, 33:6840–6851, 2020.
- ⁵⁸E. R. Beyerle. thermomaps-gayberne. <https://github.com/erb24/thermomaps-gayberne>, 2024.
- ⁵⁹Roger A. Horn and Charles R. Johnson. *Matrix Analysis*. Cambridge University Press, New York, NY, USA, 1986.
- ⁶⁰Dwaipayan Chakrabarti and Biman Bagchi. Energy landscape view of phase transitions and slow dynamics in thermotropic liquid crystals. *Proceedings of the National Academy of Sciences*, 103(19):7217–7221, 2006.
- ⁶¹Aidan P Thompson, H Metin Aktulga, Richard Berger, Dan S Bolintineanu, W Michael Brown, Paul S Crozier, Pieter J In’t Veld, Axel Kohlmeyer, Stan G Moore, Trung Dac Nguyen, et al. Lammmps-a flexible simulation tool for particle-based materials modeling at the atomic, meso, and continuum scales. *Computer Physics Communications*, 271:108171, 2022.
- ⁶²Wataru Shinoda, Motoyuki Shiga, and Masuhiro Mikami. Rapid estimation of elastic constants by molecular dynamics simulation under constant stress. *Phys. Rev. B*, 69:134103, Apr 2004.
- ⁶³I.T. Jolliffe. *Principal Component Analysis*. Springer Series in Statistics. Springer, 2002.
- ⁶⁴Diederik P Kingma and Max Welling. Auto-encoding variational bayes. *arXiv preprint arXiv:1312.6114*, 2013.
- ⁶⁵Pauli Virtanen, Ralf Gommers, Travis E. Oliphant, Matt Haberland, Tyler Reddy, David Cournapeau, Evgeni Burovski, Pearu Peterson, Warren Weckesser, Jonathan Bright, Stéfan J. van der Walt, Matthew Brett, Joshua Wilson, K. Jarrod Millman, Nikolay Mayorov, Andrew R. J. Nelson, Eric Jones, Robert Kern, Eric Larson, C J Carey, İlhan Polat, Yu Feng, Eric W. Moore, Jake VanderPlas, Denis Laxalde, Josef Perktold, Robert Cimrman, Ian Henriksen, E. A. Quintero, Charles R. Harris, Anne M. Archibald, Antônio H. Ribeiro, Fabian Pedregosa, Paul van Mulbregt, and SciPy 1.0 Contributors. SciPy 1.0: Fundamental Algorithms for Scientific Computing in Python. *Nature Methods*, 17:261–272, 2020.
- ⁶⁶John Taylor. *Introduction to error analysis, the study of uncertainties in physical measurements*. University Science Books, 1997.
- ⁶⁷Brian Cowan. *Topics in Statistical Mechanics*. Imperial Science Press, 2005.
- ⁶⁸Roberto Berardi, Andrew P. J. Emerson, and Claudio Zannoni. Monte carlo investigations of a gay—berne liquid crystal. *J. Chem. Soc., Faraday Trans.*, 89:4069–4078, 1993.
- ⁶⁹Claudio Zannoni. From idealised to predictive models of liquid crystals. *Liquid Crystals*, 45(13-15):1880–1893, 2018.
- ⁷⁰C.M. Bishop and H. Bishop. *Deep Learning: Foundations and Concepts*. Springer International Publishing, 2023.
- ⁷¹Murty SS Challa, David P Landau, and K Binder. Finite-size effects at temperature-driven first-order transitions. *Physical Review B*, 34(3):1841, 1986.
- ⁷²Kurt Binder. Computer simulations of critical phenomena and phase behaviour of fluids. *Molecular Physics*, 108(14):1797–1815, 2010.
- ⁷³James M Polson and Daan Frenkel. First-order nematic-smectic phase transition for hard spherocylinders in the limit of infinite aspect ratio. *Physical Review E*, 56(6):R6260, 1997.
- ⁷⁴Zhisheng Xiao, Qing Yan, and Yali Amit. Exponential tilting of generative models: Improving sample quality by training and sampling from latent energy. *arXiv preprint arXiv:2006.08100*, 2020.
- ⁷⁵Naruo Ohga and Sosuke Ito. Inferring nonequilibrium thermodynamics from tilted equilibrium using information-geometric legendre transform. *Phys. Rev. Res.*, 6:013315, Mar 2024.